

FIRST RESULTS OF THE COBE SATELLITE MEASUREMENT OF THE ANISOTROPY OF THE COSMIC MICROWAVE BACKGROUND RADIATION

G. F. Smoot,¹ C. L. Bennett,² A. Kogut,³ J. Aymon,¹
C. Backus,⁴ G. de Amici,¹ K. Galuk,⁴ P. D. Jackson,⁴
P. Keegstra,⁴ L. Rokke,⁴ L. Tenorio,¹ S. Torres,⁴ S. Gulkis,⁵
M. G. Hauser,² M. Janssen,⁵ J. C. Mather,² R. Weiss,⁶
D. T. Wilkinson,⁷ E. L. Wright,⁸ N. W. Boggess,²
E. S. Cheng,² T. Kelsall,² P. Lubin,⁹ S. Meyer,⁶
S. H. Moseley,² T. L. Murdock,¹⁰ R. A. Shafer² and R. F. Silverberg²

¹Lawrence Berkeley Laboratory and Space Sciences Laboratory,
University of California, Berkeley; ²Laboratory for Astronomy and
Solar Physics, NASA, Goddard Space Flight Center;

³National Research Council, NASA/GSFC; ⁴ST Systems Inc.;

⁵NASA Jet Propulsion Laboratory, Pasadena;

⁶Massachusetts Institute of Technology; ⁷Princeton University;

⁸University of California, Los Angeles; ⁹University of California,
Santa Barbara; ¹⁰General Research Corporation, U.S.A.

ABSTRACT

We review the concept and operation of the Differential Microwave Radiometers (DMR) instrument aboard NASA's Cosmic Background Explorer (COBE) satellite, with emphasis on the software identification and subtraction of potential systematic effects. We present preliminary results obtained from the first six months of DMR data and discuss implications for cosmology.

INTRODUCTION

The cosmic microwave background (CMB) is the most accessible relic from the era over which the universe has evolved from a relatively structureless plasma to the highly-ordered state observed today. In standard models of cosmology, CMB photons have travelled unhindered from the surface of last scattering in the early universe to the present era; as such, the CMB maps the large scale structure of space-time in the early universe. Despite a quarter-century of effort, no intrinsic anisotropy in the CMB has been detected.

The Differential Microwave Radiometers (DMR) instrument aboard NASA's Cosmic Background Explorer (COBE)* satellite is intended to provide precise maps of the microwave sky on large angular scales, limited only by instrument sensitivity and integration time. It consists of six differential microwave radiometers, two independent radiometers at each of three frequencies: 31.5, 53, and 90 GHz (wavelengths 9.5, 5.7, and 3.3 mm). These frequencies encompass a window in which the CMB dominates foreground galactic emission by at least a factor of roughly 1000. The multiple frequencies allow subtraction of galactic emission using its spectral signature, yielding maps of the CMB and thus the distribution of matter and energy in the early universe. Each radiometer measures the difference in microwave power between two regions of the sky separated by 60°. The combined motions of spacecraft spin (75 s period), orbit (103 minute period), and orbital precession (~1 degree per day) allow each sky position to be compared to all others through a massively redundant set of all possible difference measurements spaced 60° apart.

* The National Aeronautics and Space Administration/Goddard Space Flight Center is responsible for the design, development, and operation of the Cosmic Background Explorer. GSFC is also responsible for the software development through to the final processing of the space data. The COBE program is supported by the Astrophysics division of NASA's Office of Space Science and Applications.

A software analysis system receives data telemetered from the satellite, determines the instrument calibration, and inverts the difference measurements to map the microwave sky in each channel. Although the experiment has been designed to minimize or avoid sources of systematic uncertainty, both the instrument and the software can potentially introduce systematic effects correlated with antenna pointing, which would create or mask features in the final sky maps. In the following sections we discuss the ability of the DMR to distinguish systematic artifacts from cosmological signals, present preliminary results from the first six months of operation, and discuss some implications of these results for cosmology.

INSTRUMENT DESCRIPTION AND OPERATION

Each radiometer consists of a superheterodyne receiver switched at 100 Hz between two identical corrugated horn antennas. The antennas, designed for low sidelobes and compact size, have a main lobe well described by a Gaussian profile with 7° FWHM and are pointed 60° apart, 30° to either side of the spacecraft spin axis [1]. The two channels at 31.5 GHz share a single antenna pair with an orthomode transducer splitting the input into opposite circular polarizations. A single local oscillator provides a common reference signal to independent mixer-preamp assemblies for the two channels at each frequency. The signals in each channel undergo further amplification, detection, synchronous demodulation, and 0.5 s integration before being digitized and stored in an on-board recorder. Both channels share a common enclosure and thermal regulation system. The 53 and 90 GHz radiometers are similar but have two antenna pairs at each frequency, each with identical linear polarization response. A detailed description of the DMR instrument may be found in Smoot *et al.* [2].

Small imbalances between the two arms of each radiometer generate an instrumental baseline even when the two antennas receive identical amounts of power from the sky. Changes in the radiometer (e.g., amplifier temperature or local oscillator frequency drifts) can modulate this instrumental signature. In addition, the on-board digitization stores the output voltage as a 12-bit positive integer, mapping ± 4 K instrument signal to the range [0,4095] and in effect adding a constant of 2048 digital units (du) to the

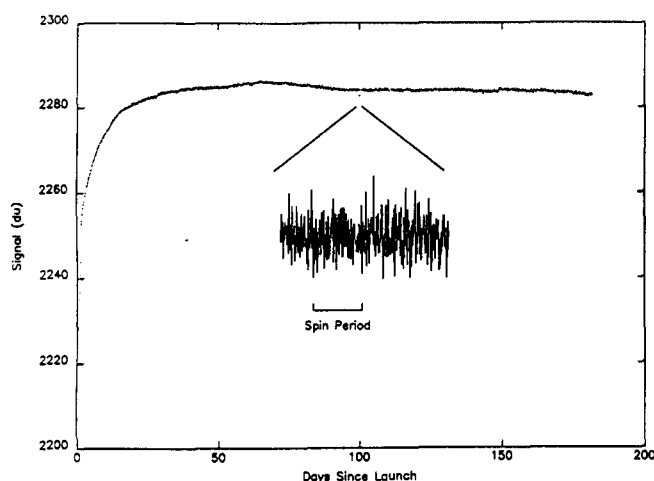


Figure 1. Uncalibrated differential temperature from the 53B radiometer for six months following launch. Each datum is the average of the radiometer output over a 103-minute orbit. The inset shows details of the short-term structure over a 4-minute period.

instrument baseline. Figure 1 shows the differential signal from the 53B channel for a six-month period following launch. The rapid rise immediately after launch reflects the expected cooling of components to orbital conditions. The baseline then stabilizes in the orbital environment and remains constant thereafter within 6 mK over six months. As the spacecraft rotates, the antennas interchange position on the sky every 38 seconds. This interchange enables celestial anisotropies, which change sign upon instrument rotation, to be distinguished from instrumental imbalances, which do not. The switching at spin, orbital, and longer periods provides a powerful tool to separate sky signals from instrumental effects.

Solid-state noise sources provide in-flight calibration by injecting broad-band microwave power into the front end of each radiometer at regular intervals (every two hours). All radiometers are calibrated simultaneously. There are two noise sources for each frequency; each noise source is coupled to both channels. One noise source injects broad-band microwave power into the positive arm and the other to the negative arm. Fired sequentially, they provide an approximate square-wave reference pulse (Figure 2). Details of pulse shape are unimportant provided the pulses are repeatable and receive identical analysis during ground tests and in orbit.

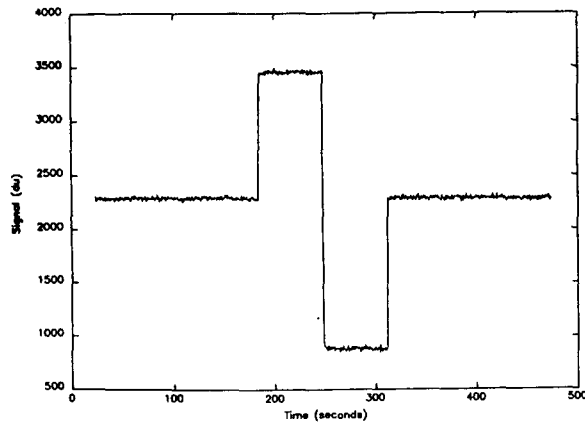


Figure 2. Uncalibrated differential temperature from the 53B radiometer during a noise source calibration sequence.

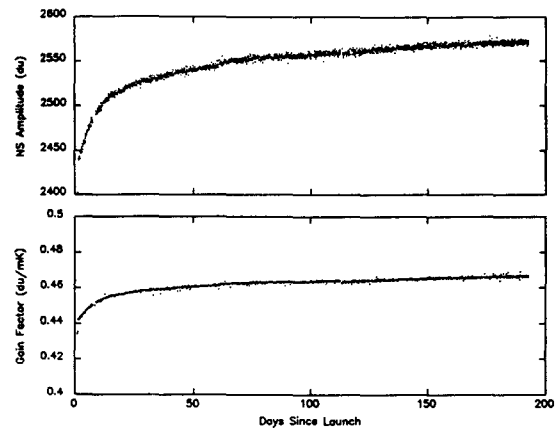


Figure 3. Noise source signal amplitude and derived calibration factor for the 53B radiometer for six months following launch.

Laboratory tests prior to launch determined the power emitted by each noise source by comparing the noise source signal to the signal produced by covering the antenna apertures with targets of known, dissimilar temperatures (approximately 300 K and 77 K). A series of such tests at different noise diode temperatures established the thermal dependence of the noise source power; the effect is generally negligible. The noise sources provide a transfer standard of ground tests to flight conditions provided the noise sources remain stable in orbit. By comparing a single noise source observed in both channels to both noise sources observed in a single channel, changes in radiometer calibration can be distinguished from changes in noise source performance.

Figure 3 shows the noise source square-wave amplitudes and corresponding derived calibration factor for the 53B channel for six months following launch. The noise source square-wave amplitude is the product of the microwave power and the radiometer calibration; the rapid drift immediately after launch reflects the expected large temperature changes as components stabilized to flight conditions.

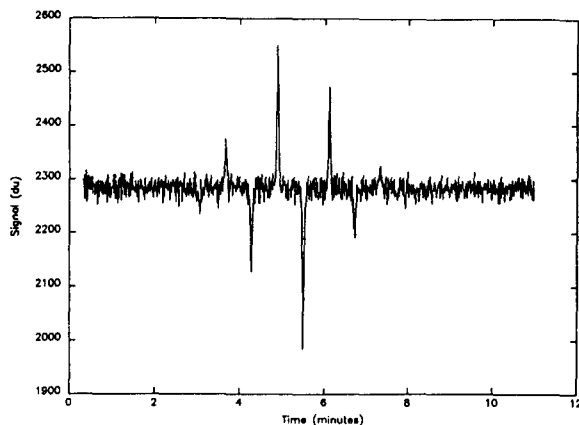


Figure 4. Uncalibrated differential temperature from the 53B radiometer. The spacecraft spin allows the two antennas alternately to view the Moon, while the orbital motion sweeps the antenna beam pattern over the Moon.

Several celestial sources provide an independent determination of the calibration factor. The DMR observes the Moon for a fraction of an orbit two weeks of every month. Figure 4 shows the output of the 53B channel during a ten-minute observation of the Moon. The lunar signal is the product of the antenna beam pattern, radiometer calibration, and lunar microwave emission. Given knowledge of the antenna pointing, beam pattern, and a model of lunar emission, the calibration factor can be deduced. This method is limited primarily by knowledge of the lunar emission, but serves as a useful check on the absolute calibration of the DMR instrument. The Moon also serves as a precise check on any changes in noise source performance. The lunar signal at constant phase provides a stable external source to which the relative internal noise source performance may be referred.

The Earth's motion about the solar system barycenter provides a second independent determination of the calibration factor. The $\sim 30 \text{ km s}^{-1}$ motion produces a Doppler-shift dipole of known magnitude

(~ 0.3 mK) and direction. Figure 5 shows the effect through the first six months of data. The modulation in amplitude and direction is apparent, but at low signal to noise. Given sufficient observing time (approximately one year), this method may produce the most accurate determination of the absolute calibration of the DMR instrument. The DMR calibration will be discussed more fully in a forthcoming paper [3].

COBE was launched on November 18, 1989 into a 900-km circular, near-polar orbit (inclination 99°). The Earth's gravitational quadrupole moment precesses the orbit to follow the terminator, allowing the instruments to point away from the Earth and perpendicular to the Sun to avoid both solar and terrestrial radiation. Throughout most of the year, the satellite orbit provides an exceptionally stable environment. During the two months surrounding summer solstice, the satellite is unable to shield from the Earth and Sun simultaneously, and the Earth limb becomes visible over the shielding surrounding the instrument aperture plane as the satellite passes over the North Pole. During the same period, the satellite enters the Earth's shadow as the orbit crosses over the South Pole. The resultant eclipse modulates both the spacecraft temperatures (removing the heat input from the Sun) and bus voltages (running on batteries while solar panels are inoperative).

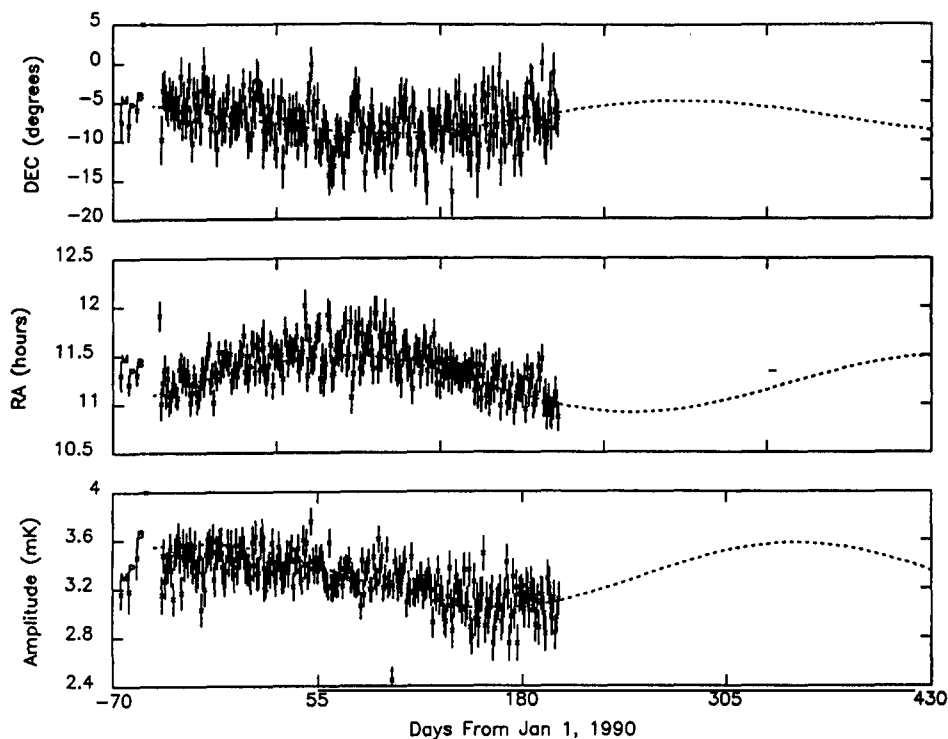


Figure 5. Amplitude and direction of the dipole anisotropy observed by the 53B radiometer each day for six months following launch. Systematic effects and galactic emission have not been removed from the data prior to fitting a dipole anisotropy.

DATA REDUCTION AND ANALYSIS

Description of Data Processing

Data from the COBE satellite are digitized and stored in an on-board tape recorder before being telemetered daily to a ground station. A pre-processor strips the DMR data from the telemetry stream and writes a raw data archive. A second processor merges the raw DMR data with spacecraft attitude and orbit information and checks the quality of the data, flagging data known or suspected to be unusable. Data of questionable telemetry quality are flagged, as are data without accompanying attitude information or spurious data written with the instrument science telemetry disabled. This accounts for less than 1% of the data. The processor flags spikes and transients in the data, discarding all points that lie more than five

times the RMS scatter from the daily mean ($< 0.1\%$ of the data). There are no known celestial sources other than the Moon that would exceed this limit. Finally, the processor flags the data for the presence in the main beam of various celestial sources (e.g., the Moon) which could contaminate the data. The results presented below discard all data with the Moon closer than 25° to an antenna. The merged, flagged data are then written to a second time-ordered archive.

A calibration program uses the estimated noise source emitted power and the in-flight square-wave calibration signal to determine the radiometer calibration factor. The noise sources provide calibration pulses every two hours; the calibration program interpolates smoothly between calibrations and writes the result to the time-ordered archive. The mean baseline, smoothed over a 4-hour period, is also written to archive. To preserve data integrity and allow for future refinements in baseline and calibration estimation, the time-ordered archive carries the baseline and calibration factor separately and does not explicitly correct and overwrite the raw data. A sky map program then subtracts the baseline, calibrates each datum, and corrects the differential signal to the solar system barycenter. The results presented below contain no other corrections. A sparse matrix algorithm varies the temperatures of 6144 map pixels independently to provide a least-squares fit to the data. The pixel size is approximately $3'$, smaller than the $7'$ DMR beam; consequently, there is some correlation between neighboring pixels for sources in the sky. Further details of the data processing algorithms may be found in Torres *et al.* [4].

Limits on Potential Systematics

The sky maps produced by the sparse matrix algorithm may in principle contain contamination from local sources or artifacts from the data reduction process itself. Effects which are systematically correlated with antenna pointing or orbital period will appear preferentially in certain pixels and will not average down as the instrument accumulates more data. The data reduction process must distinguish cosmological signals from a variety of potential systematic effects. These can be categorized into several broad classes.

The most obvious source of non-cosmological signals is the presence in the sky of foreground microwave sources. These include thermal emission from the COBE spacecraft itself, from the Earth, Moon, and Sun, and from other celestial objects. Non-thermal radio-frequency interference (RFI) must also be considered, both from ground stations and from geosynchronous satellites. Although the DMR instrument is largely shielded from such sources, their residual or intermittent effect must be considered. A second class of potential systematics is the effect of the changing orbital environment on the instrument. Various instrument components have slightly different performance with changes in temperature, voltage, and local magnetic field, each of which can be modulated by the COBE orbit. Longer-term drifts can also affect the data. Finally, the data reduction process itself may introduce or mask features in the data. The DMR data are differential; the sparse matrix algorithm is subject to concerns of both coverage (closure) and solution stability. Other features of the data reduction process, particularly the calibration and baseline subtraction, are also a source of potential artifacts. All potential sources of systematic error must be identified and their effects measured or limited before maps with reliable uncertainties can be produced.

A variety of techniques exist to identify potential systematics and place limits on their effects. For the case of known celestial sources or geosynchronous RFI, the mapping program can produce a sky map in appropriate object-centered coordinates. The contribution of the source at a given distance from beam center can be read directly from the maps to the noise limit. Spike detection and direct inspection of the data during satellite telemetry transmission limit the effects of asynchronous or intermittent RFI. Limits to the effect of diffracted terrestrial radiation can be obtained by subtracting sky maps produced near summer solstice (with the Earth limb above the shielding) from maps of similar sky coverage and integration time, obtained when the Earth is below the shield. The degree to which the subtracted maps differ from Gaussian noise provides an estimate of the effect of the differential terrestrial signal. Based on this analysis, the combined limit for local foreground contribution to the six-month maps is $\Delta T < 0.15$ mK (95% confidence level).

Systematics associated with environmental effects (e.g., instrument magnetic, thermal, and voltage susceptibilities) typically are modulated at orbital or longer periods. Although these susceptibilities have been measured prior to launch, we desire a direct comparison of the effect in orbit with that measured on the ground. The sparse matrix mapping program has the capability for simultaneous least-squares fitting to both the pixels and specified models for systematics. Over a six month period, the orbital inclination and precession combine to decouple orbit-related effects from large-scale structure on the sky. Magnetic effects appear in the maps primarily as power in low-order spherical harmonics. A least-squares fit to six months of data yields a limit to magnetic artifacts of $\Delta T < 0.17$ mK.

A least-squares analysis is ideal for magnetic susceptibility as the spacecraft sweeps through the Earth's known field each orbit. It is of only limited use for thermal or voltage susceptibilities, since the normal orbital variation in these signals is below the digitization limit of the temperature and voltage sensors. For these effects, the sharp increase in variation during seasonal eclipses over the South Pole provide a useful upper limit. Figure 6 shows a time sequence before and during the eclipse season. The top trace shows the temperature of the instrument power distribution box, whose temperature was not regulated during flight. As the eclipses start, the mean temperature falls and develops a pronounced orbital modulation of nearly 2 K (insets). Since the voltage undergoes further regulation downstream of the power distribution units, the differential output of each radiometer is sensitive primarily to the temperatures of the RF chain inside a thermally-controlled enclosure. The middle trace shows the temperature of the 53B lock-in amplifier, whose temperature was controlled by an active system during flight. The overall cooling is very slight (0.01 K) and shows minimal orbital variation. The differential output of the radiometer has a small thermal dependence upon a minimally-varying signal. The bottom trace of Figure 6 shows the differential signal from the 53B radiometer. The baseline shows no obvious evidence of additional power at the orbital period during the eclipse season. We conclude that orbital thermal and voltage variations during eclipses perturb the output by $\Delta T < 0.12$ mK during seasonal eclipses, and are < 0.01 mK during the rest of the year when stability improves a factor of ten or more.

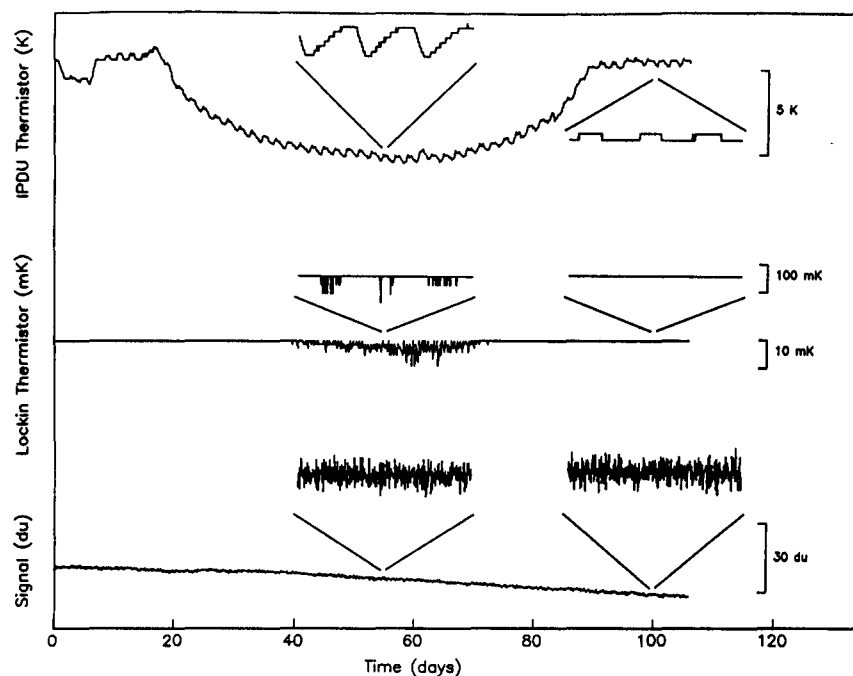


Figure 6. IPDU thermistor (top trace), lockin amplifier thermistor (middle trace) and uncalibrated differential temperature (bottom trace) from the 53B radiometer for four months surrounding the seasonal eclipses. Insets show details over several orbits. The effects of orbital eclipses can be seen as the expected long-term cooling and orbital modulation of the spacecraft (IPDU) temperatures. The lockin temperature shows only slight modulation; no effect is apparent for the radiometer output.

The extent to which the data reduction process itself may introduce artifacts in the sky maps is not readily susceptible to analytic solution. Examples include the stability of the sparse matrix solution in the presence of noise and signals that do not sum to zero over a closed pixel path (e.g., drifts). Instead, we use Monte Carlo simulations to test the solution stability and its ability to correctly identify various initial random patterns on the sky. We conclude that the sparse matrix algorithm is robust and capable of recovering the input sky map with uncertainties consistent with the Gaussian instrument noise per pixel.

A further concern is the interaction of baseline and gain estimation on different time scales than downstream processing. We currently estimate the gain and baseline daily, while processing many days at a time through the sparse matrix routine. Signals systematically correlated with pointing and orbit may be able to propagate through the software if the effects are present daily but at too low a signal-to-noise ratio to be removed in the baseline or gain estimation. The effects may not average to zero as additional data accumulated and could eventually produce artifacts in the sky maps. To estimate the propagation of such effects, we run the entire software system using simulated data containing known signals at low S/N, and compare the resultant maps to maps produced with inputs identical but for the signal under investigation.

Table 1 summarizes current limits to potential systematics. The results in many cases are limited by sky coverage, signal to noise, and available analysis software. We anticipate increasingly tighter limits to potential systematics as coverage, integration time, and software improve.

TABLE 1 95% C.L. Upper Limits to Potential Systematic Effects

Foreground Emission	Peak Magnitude	Magnitude in Maps
COBE shield and dewar	<0.04 mK	<0.002 mK
Earth	<0.3 mK	<0.07
Moon (>25 degrees)	<0.04 mK	<0.02
Sun	<0.03 mK	<0.02
Planets	<0.26 mK	<0.26 a
Galaxy	<0.3 mK	<0.13 b
Extragalactic	<0.02 mK	<0.01
Orbit Environment	Peak Magnitude	Magnitude in Maps
Magnetic	<0.3 mK/G	<0.17
Thermal	<20 mK/K	<0.01
Voltage	<20 mK/V	<0.01
Cross-talk	<2 mK	<0.0001
Software Artifacts	Peak Magnitude	Magnitude in Maps
Solution Stability	<10 ⁻⁶	<0.0001
Baseline Residuals	<2 mK	<0.03
Calibration Residuals	<2 %	<0.06
Absolute Calibration	<5 %	<0.17 c
Antenna Pointing	<1°	<0.03
Total Systematics		<0.24 mK

a Effect limited to one pixel

b Excluding data within 10° of galactic plane

c Dipole term only

RESULTS

Figure 7 shows preliminary maps of the microwave sky for each of the six DMR channels. The independent maps at each frequency enable celestial signals to be distinguished from noise or spurious features: a celestial source will appear at identical amplitude in both maps. The three frequencies allow separation of cosmological signals from local (galactic) foregrounds based on spectral signatures. The maps have been corrected to solar-system barycenter and do not include data taken with an antenna closer than 25° to the Moon; no other systematic corrections have been made. All six maps clearly show the dipole anisotropy and galactic emission. The dipole appears at similar amplitudes in all maps while galactic emission decreases sharply at higher frequencies, in accord with the expected spectral behavior.

An observer moving with velocity $\beta = v/c$ relative to an isotropic radiation field of temperature T_0 observes a Doppler-shifted temperature

$$\begin{aligned} T &= T_0 \frac{(1 - \beta^2)^{1/2}}{1 - \beta \cos(\theta)} \\ &= T_0 \left[1 + \beta \cos(\theta) + \frac{1}{2} \beta^2 \cos(2\theta) + O(\beta^3) \right] \end{aligned} \quad (1)$$

The first term is the monopole CMB temperature without a Doppler shift. The second term, proportional to β , is a dipole distribution, varying as the cosine of the angle between the velocity and the direction of observation. The term proportional to β^2 is a quadrupole, varying with cosine of twice the angle with amplitude reduced by $1/2 \beta$ from the dipole amplitude. The DMR maps clearly show a dipole distribution consistent with a Doppler-shifted thermal spectrum, implying a velocity for the solar system barycenter of $\beta = 0.00122 \pm 0.00003$ (68% CL), or $v = 366 \pm 10 \text{ km s}^{-1}$ toward $(l, b) = (264^\circ \pm 2^\circ, 49^\circ \pm 2^\circ)$, where we assume a value $T_0 = 2.735 \text{ K}$. The solar system velocity with respect to the local standard of rest is estimated at 20 km s^{-1} toward $(57^\circ, 23^\circ)$, while galactic rotation moves the the local standard of rest at 220 km s^{-1} toward $(90^\circ, 0^\circ)$ /5,6/. The DMR results thus imply a peculiar velocity for the Galaxy of $v_g = 545 \pm 10 \text{ km s}^{-1}$ in the direction $(266^\circ \pm 2^\circ, 30^\circ \pm 2^\circ)$. This is in rough agreement with independent determinations of the velocity of the local group, $v_{lg} = 507 \pm 10 \text{ km s}^{-1}$ toward $(264^\circ \pm 2^\circ, 31^\circ \pm 2^\circ)$ /7/.

Figure 8 shows the DMR maps with this dipole removed from the data. The only large-scale feature remaining is galactic emission, confined to the plane of the galaxy. This emission is present at roughly the level expected before flight and is consistent with emission from electrons (synchrotron and HII) and dust within the galaxy. The ratio of the dipole anisotropy (the largest cosmological feature in the maps) to the Galactic foreground reaches a maximum in the frequency range 60—90 GHz. There is no evidence of any other emission features.

We have made a series of spherical harmonic fits to the data, excluding data within several ranges of galactic latitude. The only large-scale anisotropy detected to date is the dipole. Quadrupole and higher-order terms are limited to amplitude $\Delta T/T < 10^{-4}$. Similarly, a search for Gaussian or non-Gaussian fluctuations on the sky showed no features to limit $\Delta T/T < 10^{-4}$. The results are insensitive to the precise cut in galactic latitude and are consistent with the expected Gaussian instrument noise. The reported uncertainties are 95% confidence level unless otherwise stated, and include the effects of systematics as listed in Table 1.

DISCUSSION

The DMR limits to CMB anisotropies provide significant new limits to the dynamics and physical processes in the early universe. The dipole anisotropy provides a precise measure of the Earth's peculiar velocity with respect to the co-moving frame. Limits to higher-order anisotropies limit global shear and vorticity in the early universe. If the universe were rotating (in violation of Mach's Principle), the

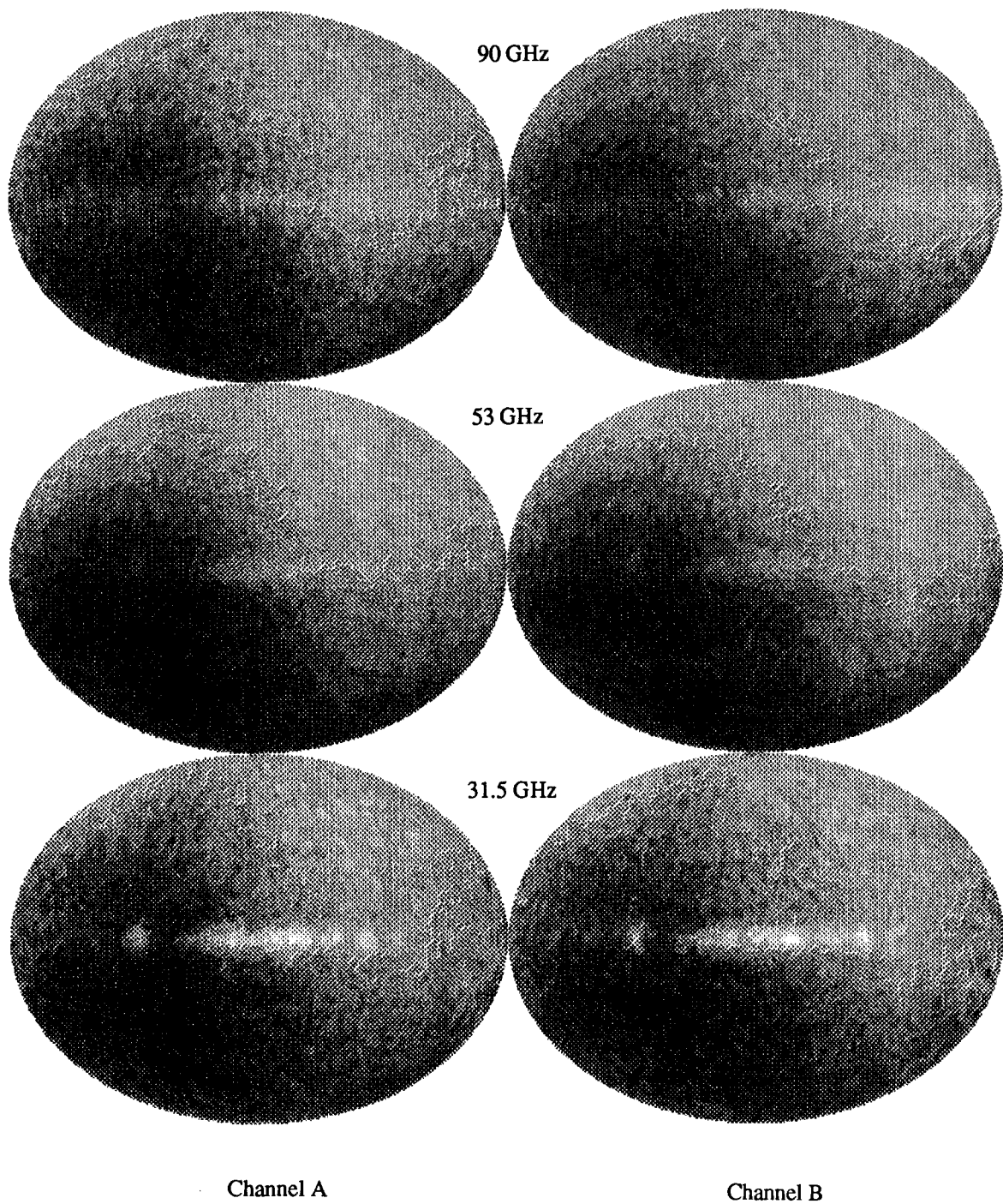


Figure 7. COBE DMR full sky maps of the relative temperature of the sky at frequencies 31.5, 53.0, and 90.0 GHz. The maps are in galactic coordinates and have been corrected to solar system barycenter. The maps show variations in received power and are insensitive to the mean temperature of about 2.735 K.

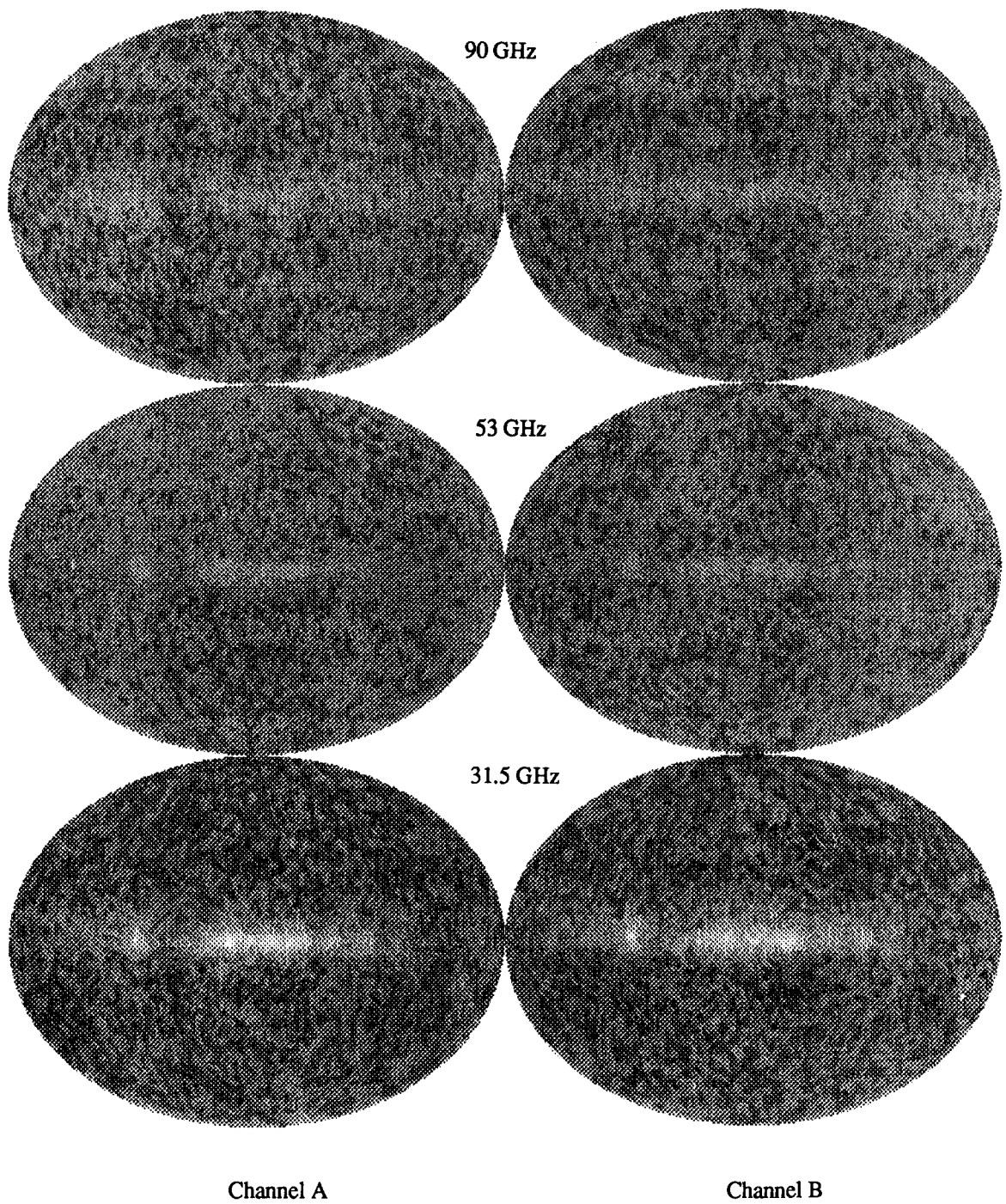


Figure 8. COBE DMR full sky maps at frequencies 31.5, 53.0, and 90.0 GHz. A dipole anisotropy corresponding to a motion of 370 km/s through a 2.735 K blackbody has been subtracted from the maps shown in Figure 7.

resultant metric causes null geodesics to spiral; in a flat universe the resultant anisotropy is dominated by a quadrupole term /8,9/. The limit $\Delta T/T < 10^{-4}$ for quadrupole and higher spherical harmonics limits the rotation rate of universe to $\Omega < 3 \times 10^{-24} \text{ s}^{-1}$, or less than one ten-thousandth of a turn in the last ten billion years.

If the expansion of the universe were not uniform, the expansion anisotropy would lead to a temperature anisotropy in the CMB of similar magnitude. The large-scale isotropy of the DMR results indicate that the Hubble expansion is uniform to one part in 10^4 . This provides additional evidence for hot big bang models of cosmology, and indicates that the currently observed expansion of the universe can be traced back at least to the radiation-dominated era.

Inhomogeneities in the density in the early universe also lead to temperature anisotropies in the CMB as the CMB photons climb out of varying gravitational potential wells /10,11/

$$\Delta T/T \sim \frac{1}{2} \frac{\delta \rho}{\rho} \left(\frac{H_0 L}{c} \right)^2 \quad (2)$$

The DMR results imply that the universe at the surface of last scattering was isotropic and homogeneous to the 10^{-4} level. The results have implications for structures beyond the present Hubble radius: on large scales the universe is isotropic and homogeneous. The large scale geometry of the universe is thus well-described by a Robertson-Walker metric with only local perturbations.

One such potential local perturbation is gravitational radiation. Long-wavelength gravitational waves propagating through this region of the universe distort the metric and produce a quadrupole distortion in the CMB. For a single plane wave the resultant CMB anisotropy is

$$\Delta T/T \sim \frac{1}{2} (A_r - A_e) (1 - \cos(\theta)) \cos(2\phi) \quad (3)$$

where A_r and A_e are the proper strains at the emitter and receiver, respectively /12/. The DMR is sensitive primarily to gravitational waves with scale sizes $> 7^\circ$ at the surface of last scattering, or ~ 200 Mpc today. The limits $\Delta T/T < 10^{-4}$ for quadrupole and higher spherical harmonics limit the energy density of single plane waves or a chaotic superposition to

$$\Omega_{\text{GW}} < 4 \times 10^{-3} \left(\frac{\lambda_{\text{GW}}}{10 \text{ Mpc}} \right)^{-2} h^{-2} \quad (4)$$

where Ω_{GW} is the energy density of the radiation relative to the critical density, λ_{GW} is the wavelength at the current epoch, and h is the Hubble constant in units $100 \text{ km s}^{-1} \text{ Mpc}^{-1}$.

Cosmic strings provide another mechanism for local perturbations in the metric. They are nearly one-dimensional topological defects predicted by many particle physics gauge theories and are characterized by a large mass per unit length, μ /13/. The large mass and relativistic velocity produce CMB anisotropies through the relativistic boost and the Sachs-Wolfe effect (gravitational lensing alone does not produce anisotropy in an otherwise isotropic background). Many authors have calculated the anisotropy produced by various configurations of cosmic strings, with typical values /14,15/

$$\Delta T/T \sim 8\pi\beta\gamma \frac{G\mu}{c^2} \quad (5)$$

The DMR experiment limits the existence of large-scale cosmic strings to $G\mu/c^2 < 10^{-4}$. There is no evidence for higher-order topological defects such as domain walls. The large scale geometry of the universe appears to be uniform and without defects.

The observed isotropy of the universe on large angular scales presents a major problem for cosmology. At the surface of last scattering the horizon size was ~ 100 kpc ($\sim 2^\circ$). Regions separated by more than 2° were not in causal contact; consequently, DMR measures some 10^4 causally disconnected regions of the sky. Standard models of cosmology fail to explain why these regions are observed to have the same temperature to order unity, much less the 10^{-4} isotropy implied by the DMR observations. Inflationary scenarios provide one solution. In these models, the universe undergoes a spontaneous phase transition $\sim 10^{-32}$ seconds after the Big Bang, causing a period of exponential growth in which the scale size increases by 30 to 40 orders of magnitude. The entire observed universe would then originate from a small pre-inflationary volume in causal contact with itself, eliminating the problem. In the simplest inflationary models, the pre-inflationary matter and radiation fields are diluted to zero along with any pre-existing anisotropies. The process of inflation, however, generates scale-free anisotropies with a Harrison-Zel'dovich spectrum which result in small but detectable CMB anisotropies in the present universe [16,17]. Although current DMR limits are an order of magnitude above the predicted spectrum, we anticipate achieving sufficient sensitivity over the planned mission to test the predictions of inflationary models.

A second major problem in cosmology is the growth of structure in the universe. The largest structures in the current universe (walls and voids) are observed to have density fluctuations $\delta\rho/\rho$ of order unity on scale sizes ~ 50 Mpc. Structures of this size are at the horizon scale at the surface of last scattering; consequently, the primordial density fluctuations are small and most of the growth is in the linear regime. The assumption of linear growth requires peculiar velocities $\sim 0.01c$ in order to move the matter the required 10^8 light years of co-moving distance in the $\sim 10^{10}$ years estimated to have elapsed since the surface of last scattering, an order of magnitude greater than the peculiar velocity inferred from dipole anisotropy. To explain the observed structure without violating limits on CMB anisotropy, and to generate the critical density required by inflationary models, many astrophysicists have turned to cosmological models in which most of the matter in the universe ($> 90\%$) is composed of weakly interacting massive particles (WIMPs). The dynamical properties of this "dark matter" allow it to clump faster than the baryonic matter, which later falls into the WIMP gravitational potential wells to form the structures observed today. The gravitational potential and motion of these particles produce CMB anisotropy whose amplitude depends on the angular scale size. For scale size $\sim 10^\circ$ most reasonable models predict $\Delta T/T \sim 1-3 \times 10^{-5}$, depending on the average density of the universe [18]. Although current observations do not provide significant limits to these models, we anticipate that the DMR will provide a stringent test of such models as it continues to accumulate data.

CONCLUSIONS

Six months after launch, the instrument is working well and continues to collect data. The results are currently limited by instrument noise and upper limits to potential sources of systematic error. The current data show the expected dipole anisotropy, consistent with a Doppler-shifted thermal spectrum. Galactic emission is present at levels close to those expected prior to launch, and is largely confined to the plane of the galaxy. There is no evidence for any other large-scale feature in the maps. The DMR results limit CMB anisotropies on all angular scales $> 7^\circ$ to $\Delta T/T < 10^{-4}$. The results are consistent with a universe described by a Robertson-Walker metric and show no evidence of anisotropic expansion, rotation, or localized defects (strings). As sky coverage improves and the instrument noise per field of view decreases, we anticipate improved calibration, better estimates of potential systematics, and increasingly sensitive limits to potential CMB anisotropies. In principle, the DMR is capable of testing predictions of both inflationary and dark-matter cosmological models.

REFERENCES

1. Toral, M.A., *et al.*, *IEEE Transactions on Antennas and Propagation*, **37**, 171 (1989).
2. Smoot, G.F., *et al.*, *Ap. J.*, **360**, 685 (1990).
3. Bennett, C.L., *et al.*, in preparation.

4. Torres, S., *et al.*, *Data Analysis in Astronomy*, ed. Di Gesu *et al.*, Plenum Press (1990).
5. Kerr, F.J., and Lyndon-Bell, D., *MNRAS*, **221**, 1023 (1990).
6. Fich, M., Blitz, L., and Stark, A., *Ap. J.*, **342**, 272 (1989).
7. Yahil, A., Tamman, A., and Sandage, A., *Ap. J.*, **217**, 903 (1977).
8. Collins, C.B., and Hawking, S.W., *MNRAS*, **162**, 307 (1973).
9. Barrow, J.D., Juskiewicz, R., and Sonoda, D.H., *MNRAS*, **213**, 917 (1985).
10. Sachs, R.K., and Wolfe, A.M., *Ap. J.*, **147**, 73 (1967).
11. Grischuk, L.P., and Zel'dovich, Ya. B., *Sov. Astron.*, **22**, 125 (1978).
12. Burke, W.L., *Ap. J.*, **196**, 329 (1975).
13. Vilenkin, A., *Physics Reports*, **121**, 263 (1985).
14. Stebbins, A., *Ap. J.*, **327**, 584 (1988).
15. Stebbins, A., *et al.*, *Ap. J.*, **322**, 1 (1987).
16. Gorski, K., *Ap. J. Lett.* (submitted 1990).
17. Abbott, L.F., and Wise, M.B., *Ap. J. Lett.*, **282**, L47 (1984).
18. Bond, J.R. and Efstathiou, G., *Ap. J. Lett.*, **285**, L45 (1984).